

In-Field Measurement and Methodology for Modeling and Validation of Precipitation Effects on Solid-State LiDAR Sensors

Marcel Kettelgerdes^{ID} and Gordon Elger

Abstract—There is a strong demand for high fidelity sensor models which are capable of simulating realistic automotive sensor perception of Radar, LiDAR and camera sensors in real time, in order to validate advanced driving assistance functions like lane change assist (LCA), automated emergency breaking (AEB), or even path planning virtually. For central data fusion the sensor models need to deliver realistic, artificial sensor raw data. In especially, optical sensors are heavily influenced by precipitation, fog and sun irradiance. However, most LiDAR models lack the capability of replicating the impact of specific weather characteristics. Furthermore, there is – in contrast to numerous publicly available LiDAR datasets – a strong lack of datasets which are annotated with quantitative weather data such as the precipitation rate or meteorological visibility in order to develop and validate such models. Hence, within this work, an automated infrastructure is setup to measure time-correlated LiDAR and weather data to develop and calibrate weather models. The effects of varying precipitation rates on an automotive Flash LiDAR system is demonstrated based on in-field measurements and a respective modeling methodology is developed. Based on the in-field measurement data, raw data LiDAR models can be developed which augment virtual LiDAR data obtained from raytracing capable driving simulation suits as well as real data, recorded under ideal weather conditions.

Index Terms—LiDAR, adverse weather, sensor model, automotive, simulation, virtual validation, ROS, ADAS.

I. INTRODUCTION

WITH the automotive industry's dedicated roadmap towards automated driving, the responsibility for reliable environmental perception moves from the driver to the vehicle's advanced driving assistance systems (ADAS). However, with steadily growing system complexity, the required test mileage to certify new driving functions increases. The sheer physical test effort to validate safety-critical and highly complex systems, operating under an uncountable number of influencing parameters, is found to be

unrealistically high [1], [2]. Consequentially, the virtual validation and respective certification process of ADAS gradually develops to one of the major challenges to facilitate partially as well as fully automated driving. Nevertheless, a certification, which is mainly based on virtual evaluation of new driving functions, demands for high fidelity models, simulating for instance vehicle dynamics, driver behavior or environmental perception. Especially in case of the latter, there has recently been a strong development in the physics-based simulation of sensor systems, which was among others enabled by sophisticated, real-time capable raytracing engines [2]. However, these simulation tools are – for the sake of being real-time capable – strongly limited in the ability to physically simulate weather conditions like precipitation and its impact on sensor performance. This tradeoff between raytracing model accuracy and computational cost has been pointed out by several authors in the past [3], [4]. An alternative approach, often referred to as “grey-box” or medium-fidelity modeling, combines physical raytracing simulation capabilities with fast phenomenological weather models in order to attain accurate, virtual sensor raw data [2], [3], [4], [5]. In order to develop such descriptive models, extensive reference measurements with the physical sensor must be conducted. In this context, it is vital that the conditions covered in the reference measurement are consistent with the conditions, the sensor is exposed to within real world operation.

Having this in mind, an automated infrastructure setup was realized in order to collect time-correlated weather and LiDAR data over long-term measurement campaigns. The target is to create a balanced dataset, facilitating the development of empirical models, which can be used to efficiently and accurately simulate weather influences on perception sensors within driving simulation suits – or to augment real data which was recorded under ideal conditions. Opposed to previous works in this field, the focus of the research in this paper lays on a solid-state Flash LiDAR system as promising, reliable sensor solution in the future automotive, robotics, as well as urban air mobility market sector.

Accordingly, the paper is structured as follows. The next section elaborates the current scientific context by presenting and discussing related works. The third section introduces the theoretical background of empirical, weather-dependent attenuation models for LiDAR sensors and based on that, a mathematical Flash LiDAR sensor model is derived as a special case. Afterwards, the measurement setup for automated

Manuscript received 21 July 2022; revised 19 November 2022; accepted 4 January 2023. Date of publication 9 January 2023; date of current version 28 June 2023. This work was supported by the German Federal Ministry of Digital and Transport (BMDV), formerly named Federal Ministry of Transport and Digital Infrastructure (BMVI), within the Automated and Connected Driving funding Program under Grant 01MM20012G (SAVeNoW). (Corresponding author: Marcel Kettelgerdes.)

Marcel Kettelgerdes is with the Institute of Innovative Mobility, University of Applied Sciences Ingolstadt, 85049 Ingolstadt, Germany (e-mail: marcel.kettelgerdes@thi.de).

Gordon Elger is with the Connected Mobility and Infrastructure, Institute for Transportation and Infrastructure Systems (IVI), Fraunhofer Society, 85049 Ingolstadt, Germany (e-mail: gordon.elger@ivi.fraunhofer.de).

Digital Object Identifier 10.1109/JRFID.2023.3234999

data acquisition will be described. On this basis, first measurement results on precipitation induced data degradation of an automotive Flash LiDAR sensor will be presented in a qualitative as well as quantitative manner and compared to findings of similar works. Finally, the last section concludes the research and gives an outlook to future work.

II. RELATED WORKS

In fact, the significant weather impact on LiDAR sensors, especially in form of precipitation and fog, has been studied intensely within the past years. Most of the investigations were conducted in a lab surrounding in order to simulate different precipitation (or fog) conditions in a reproducible manner [6], [7], [8], [9], [10], [11], [12], [13], [14]. There, the focus was mostly laid on the comparison of LiDAR sensors from different manufacturers and less on the sensor architecture itself. Hence, most of the investigations considered well established scanning LiDAR systems.

In the surveyed works, only Kutila et al. [10] focused on the comparison of different wavelengths with respect to their robustness to fog and rain influences. Therefore, they tested sensors from Ibeo, Velodyne and Hello World (HWL). Within their evaluations, they compared the relative reduction of backscattered energy and number of detected points on a defined hard target, concluding that there is no significant difference regarding the signal attenuation behavior for the 1550 nm HWL and the 905 nm Ibeo and Velodyne LiDAR. Without focusing on differences in the sensor design, Heinzler et al. [8] investigated the performance of LiDARs from Velodyne and Valeo under lab induced fog and rain conditions and generally emphasised the increasing measurement range reduction and number of false positive detections close to the sensor. Similarly, Montalban et al. [11] tested LiDARs from Velodyne, Ouster, Livox, Cepton and Aeye under artificial rain and fog conditions. By doing so, the authors evaluated the relative backscattered energy and number of points on a defined hard target as well as in the optical channel between sensor and target (noise) under varying precipitation rates and fog densities. With a decrease in meteorological visibility, also the number of points on the target generally dropped as expected. Opposed to that, the authors encountered unexpected sensor behavior while varying the nozzle induced rain rate, which finally resulted from deviations between the natural and artificial rain drop size distribution. Within rain rates with a similar drop size distribution, however, they observed an expected decrease in number of target points and increase of intensity variation as well as noise (hence false positive detections).

Bijelic et al. [6], on the other hand, focused solely on artificial fog conditions with varying resulting meteorological visibility and conducted measurements with scanning LiDARs from Velodyne and Ibeo to evaluate the maximum measurement range and backscattered signal power. Again, the results showed a strong effect, i.e., the effective measurement range reduced from a visibility of 40 m down to 25 m. In a similar manner, Jokela et al. [9] investigated the variation of the range of scanning LiDARs from Ouster, Velodyne, Ibeo and

Cepton and obtained comparable results. In an earlier work, Hasirlioglu et al. [7] already conducted a related experiment with a scanning LiDAR from Hokuyo. Hence, they generated discrete layers of fog by successively arranged nozzles, which are activated one by one. This again resulted in a strongly decreased measurement range and an increasing number of false positive detections close to the sensor. However, the generated specific attenuation of the fog layers was approximately up to $\alpha \approx 4000 \frac{\text{dB}}{\text{km}}$, which might be unrealistically high compared to natural fog, with empirical models [15] showing an attenuation of up to $\alpha \approx 300 \frac{\text{dB}}{\text{km}}$ for dense fog with a visibility ≤ 100 m. With a similar setup, the authors evaluated the same LiDAR sensor also under lab induced rain conditions, activating discrete layers of artificial rain [14]. By doing so, the authors again observed an increasing number of false positive detections and also a growing variation in measured intensity.

One can summarize that all experimental lab setups demonstrated that fog and precipitation generally have a major impact to the LiDARs perception performance. In a target-free setup, this effect was mostly quantified with the maximum achievable measurement range and the general noise level in form of false positive detections. By using a static target, some works utilized the point density on the target as well as the relative attenuation of the backscattered signal power as quality metric. Nevertheless, the majority of works in this field are lacking validation with respect to real weather conditions, partly showing strong deviations from the expected measurement behavior. Hence, the comparability between artificially generated weather conditions and real outdoor conditions is limited, as specifically emphasised by Montalban et al. [11] and Rasshofer et al. [16]. This strongly underlines the importance of sensor testing and model validation under realistic environmental conditions.

Based on such measurements, a few works already implemented empirical and stochastic models to augment ideal sensor data (either from simulation or recorded under ideal conditions) in order to simulate precipitation impact [17], [18], [19], [20].

Goodin et al. [17] used the *Mississippi State University Autonomous Vehicle Simulator* (MAVS) to point-wise simulate range and intensity for clear conditions and postprocessed it using the empirical model for rain induced signal attenuation and an uncoupled stochastic term for simulating a rain rate dependend range measurement error. This constitutes a major simplification, since the range measurement is closely coupled to the backscattered signal intensity, as it is shown in Section III-A. Opposed to that, Hasirlioglu and Riener [20] neglected the effect of signal attenuation and focused purely on stochastically inducing false positive reflections with respect to an occurring drop size distribution. Kilic et al. [19] on the other hand considered false positive detections including the respective backscattered power as well as general signal attenuation. For that, they also utilized the occurring drop size distribution and proposed a Monte-Carlo approach to postprocess the clear condition data to simulate rain induced signal degradation. Therefore, they added raindrops as random scatterers with specific backscattering characteristics and a size, which is sampled from the known drop size distribution. In a similar

manner, Hahner et al. [18] postprocessed clear pointcloud data to simulate different fog conditions, also taking into account its volumetric backscattering as well as extinction characteristics.

In sum, many current real-time capable modeling approaches postprocess ideal simulation or measurement data, to model either one or both of the two major effects which are observed within this and previous works on sensor testing – A precipitation or fog induced signal attenuation and the occurrence of false positive detections due to direct backscattering. However, one can identify a gap between model development and the data acquisition to calibrate and validate such models. Hence, the calibration of the presented models rely fully on measurement data from previous works and was not validated with reference measurements.

The gap between lab and in-field measurement effects of weather condition motivates the design of an in-field measurement system for the development and validation of weather effect models for LiDAR systems.

III. MATHEMATICAL LiDAR MODEL

Within this section, the LiDAR equation is summarized, following Rasshofer et al. [16]. Afterwards the model is adapted to the specific case of a Flash LiDAR system.

A. The LiDAR Equation

Generally, spatial energy propagation and weather-induced attenuation can be modeled by the well-known LiDAR equation in a concise manner. It describes the backscattered, received power $P_r(L)$ at the sensor's detector for a target in a specific range L . As noted already by Zhao et al. [21], it can be derived by a convolution between the transmitted signal P_t and the spatial impulse response $H(L)$ of the respective optical channel and target:

$$P_r(L) = C_A \int_{t'=0}^{\frac{2L}{c}} P_t(t') H\left(L - \frac{ct'}{2}\right) dt' \quad (1)$$

where C_A represents a system constant with $C_A = c\eta\frac{A_r}{2}$, in which A_r represents the receiver's aperture, η the losses in the receiving optic and c the speed of light within the medium of the optical channel. The transmitted signal can be ideally modeled as a Dirac-pulse, such that it can be expressed by $P_{t,\delta}(t) = E_p\delta(t)$ with E_p being the total pulse energy. This assumption does only hold if the duration of the transmit pulse τ_p is neglectable with respect to the target range L , so that $L \gg c\tau_p$ [16]. This can be regarded as a reasonable approximation, since modern day driver circuits emit pulse lengths in the range of a few - or even below one nanosecond [22]. Nevertheless, for calculating the overall pulse energy E_p , the time signature of the pulse is assumed to be in a \sin^2 -form [16]. Hence, it can be expressed by the peak power P_0 and the half-power pulse width τ_h . Therefore, (1) simplifies to the basic LiDAR equation:

$$P_{r,\delta}(L) = C_A E_p H(L) = C_A P_0 \tau_h H(L) \quad (2)$$

Now, as indicated, $H(L) = H_T(L)H_C(L)$ can be separated into the spatial impulse response of the target H_T and the spatial impulse response of the optical channel H_C [16].

B. The Optical Channel's Spatial Impulse Response Function

The impulse response of the channel can be modeled as [16]:

$$H_C(L) = \frac{T^2(L)}{L^2} \xi(L) = \frac{e^{-2 \int_{l=0}^L \alpha(l) dl}}{L^2} \xi(L) \quad (3)$$

where $T(L)$ describes the one-way transmission loss through the transmission medium to the target. The variable $\alpha(l)$ represents the local extinction coefficient, describing differential power loss in a distance l . By that, α constitutes a key variable to describe fog or precipitation induced signal attenuation and will be further clarified in Section III-D.

Aside the local extinction coefficient, $\xi(L)$ describes the range dependent crossover function between the area A_t , which is illuminated by the transmitted laser beam, and A_r as the area which is observed by the receiver optic [16]. First definitions go back to early works from Sassen and Dodd [23] as well as Halldorsson and Langerhoic [24] and the general as well as specific closed-form equations for homogeneous, conical beams can be found there. Basically, this function depends on the specific LiDAR system design, i.e., beam geometry and distance between the optical axes. The complexity of the function increases if inhomogeneous power distribution in the transmitted beam is factored in. If opposed to that, receiver and transmitter are oriented coaxially, the function equals to 1 for every distance [16], [23], [24].

C. The Target's Spatial Impulse Response Function

As complement to $H_C(L)$, the spatial response function of the target $H_T(L)$ generally, distinguishes between the modeling of *hard* and *soft* targets, with the first describing solid objects and the latter characterizing small particles, like drops from rain and fog. Following that, for soft targets it can be defined as follows [16]:

$$H_{T,s}(L) = \beta(L) \quad (4)$$

with β being the backscattering coefficient, which, like the extinction coefficient α , will be further explained in Section III-D.

For hard targets, the spatial impulse response can be defined as follows [16]:

$$H_{T,0}(L) = \begin{cases} \beta_0 \delta(L - L_0) & \text{if } A_T \geq A_t(L_0) \\ \beta_0 \delta(L - L_0) \frac{A_T}{A_t(L_0)} & \text{if } A_T < A_t(L_0). \end{cases} \quad (5)$$

with A_T describing the area of the hard target and $A_t(L_0)$ being the cross-sectional beam area of the transmitter in the target distance L_0 . This term ensures that only the portion of the transmitted beam area and respective energy is considered which is actually intersecting with the target. By modeling it as Dirac-function it is assumed that the transmitted beam signature is not altered by the target. The differential reflectivity β_0 finally describes the reflection characteristic of the target, which depends on the target geometry, its material properties on the observed surface, as well as the transmitted beam's angle of incident [16], [25], [26].

In the automotive context, one can distinguish three general types of reflection: *diffuse*, *specular* and *retro* reflection [16].

The first describes the *diffusive reflection* behavior of rough surfaces like roads or dirt layers, from which energy is distributed approximately evenly in all directions. These surfaces can be ideally modeled as Lambert reflector with $\beta_0 = \frac{\rho}{\pi}$ and $0 < \rho \leq 1$ being the reflectivity. *Specular reflection* is a directed reflection, occurring for example on a wet street or on polished, mirror-like surfaces like glass. For LiDAR systems these surfaces bear the risk that most of the incident energy is not reflected back to the receiver, which can eventually result in target loss. Opposed to that, *retro reflective* surfaces are reflecting a major energy portion of the incident signal back to the sensor, which might lead to over-exposure of the imager. This effect can be observed on street signs, where target reflectivity ρ might become significantly larger than 10. Since, real world materials do usually not fall precisely into one of these categories and mostly combine different reflection characteristics, a more general model for the angular energy distribution of the reflected laser pulse is given by the bidirectional reflection distribution function (BRDF) [16], [25], [26].

D. Precipitation and Fog Modeling

The effect of soft targets in form of precipitation (rain, snow, hail) and fog on laser pulse transmission has been intensely investigated over the past years. As extensively summarized by Hasirlioglu et al. [27], the scattering mechanism depends on the size of the observed particle as well as on the wavelength of the observing sensor. In case of an automotive LiDAR system with a typical wavelength $850 \text{ nm} \leq \lambda \leq 1570 \text{ nm}$ [28], the predominant scattering mechanisms are Mie-scattering (particle size $D \approx \lambda$) and geometrical scattering ($D \gg \lambda$) [29]. By these well understood principles, one is able to express backscattering and extinction of the transmit signals at a single particle by the backscattering efficiency $Q_b(D)$ and the extinction efficiency $Q_{\text{ext}}(D)$, respectively. Both efficiencies are depending on the wavelength of the incident light as well as on the size of the particle. In Fig. 1, the extinction efficiency is plotted for commonly utilized LiDAR wavelengths in the automotive domain. One can clearly see that for all wavelengths, the scattering behavior with respect to fog (Mie-region) and rain (region of geometrical optics) is quite similar – With a strong particle size dependency of Q_{ext} in the Mie-region and converging towards $Q_{\text{ext}} = 2$ in the geometrical region. This underlines the observation of Kuttila et al. [10], according to which the relative signal attenuation of a LiDAR operating with 1550 nm and 905 nm are similar. For detailed calculation of the extinction and backscattering efficiency, the interested reader is referred to the respective literature [29], [30].

Nevertheless, single particle models are not sufficient to explain macroscopic precipitation or fog, which is characterized by a spatial distribution of different particle sizes (and velocities). Consequentially, these macroscopic effects are modeled as volumetric targets in the form of particle size distributions $N(D)$, often referred to drop size distributions (DSD) in case of rain. There are numerous authors who published statistical models to describe the respective distributions of several precipitation types, like snow or

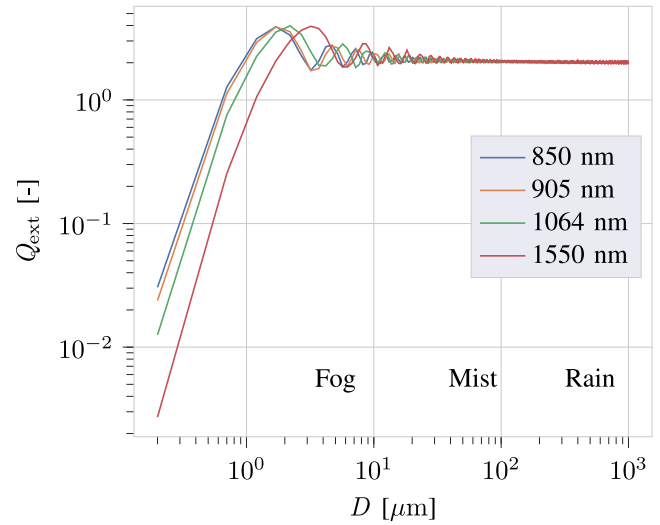


Fig. 1. Extinction efficiency Q_{ext} over particle diameter D in case of liquid precipitation and fog for common LiDAR wavelengths. While Q_{ext} shows a strong particle size dependence in the Mie-region (fog), it is converting towards $Q_{\text{ext}} = 2$ in the region of geometrical optics.

continental as well as coast rain for varying precipitation rates R [31], [32], [33], [34].

Now, the respective extinction coefficient α and backscattering coefficient β can be calculated as integral of the respective distribution and efficiency over the particle size [35]:

$$\alpha = \frac{\pi}{4} \int_{D=0}^{\infty} D^2 Q_{\text{ext}}(D) N(D) dD \quad (6)$$

$$\beta = \frac{\pi}{4} \int_{D=0}^{\infty} D^2 Q_b(D) N(D) dD \quad (7)$$

While with α , the range dependent signal extinction can be modeled, β allows for simulating the optical noise introduced by volumetric backscattering from small particles in the optical channel and can be superpositioned and compared to the hard target response β_0 by adding the impulse response functions $H_T(L) = H_{T,0}(L) + H_{T,s}(L)$, like done in [36]. Both terms highlight the importance of a precise replication of natural drop size distributions if precipitation is emulated in the lab. Although the extinction efficiency itself is, for typical LiDAR wavelengths and in case of rain, not sensitive to the particle size, it is multiplied with its squared as well as with its DSD to finally determine the extinction coefficient. Consequentially, small deviations from natural precipitation characteristics can cause unexpected signal extinction, as observed by earlier works (see Section II, [11], [16]).

E. Model Adaptation for Flash LiDAR Systems

Based on the general LiDAR model, a mathematical model for the special case of Flash LiDAR systems can be derived as an extension to similar previous works [37], [38], in which the influence of lens distortion in the receiver optic was yet not considered and weather impact was discussed in a limited, less general manner.

The Flash LiDAR system is a non-scanning sensor which illuminates the full field of view by one single, spatially expanded transmit pulse. On the receiver side, a converging

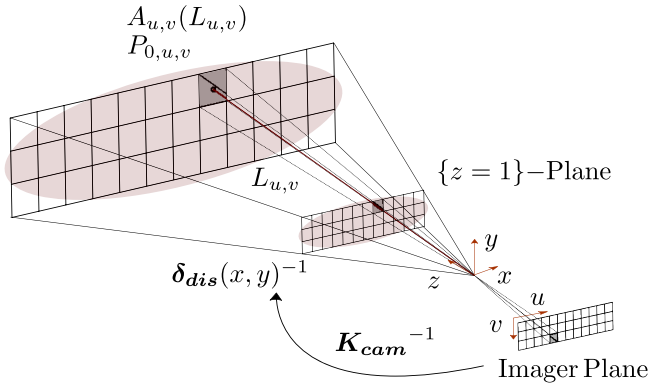


Fig. 2. Projective Flash LiDAR model. Assuming full crossover, the illuminated area $A_{t,u,v}(L_{u,v})$ per detector element (u, v) can be assumed as the respective observed area $A_{u,v}(L_{u,v})$ and hence, calculated as a function of the inverse intrinsic camera model $\{K_{cam}^{-1}, \delta_{dis}^{-1}\}$ and the target distance $L_{u,v}$.

lens is used to project the reflected energy to a photodetector array in which for each photosensitive element, a time-of-flight measurement is conducted. Since, the geometric projection is similar to that of a usual camera, also the respective model can be utilized (see Fig. 2). Hence, it can be described by the so-called *intrinsic* camera model, which is basically consisting of a linear transformation K_{cam} and a nonlinear function δ_{dis} , modeling the linear camera projection and nonlinear lens distortion, respectively [39]. This model has already been object to earlier research in context of a solid-state LiDAR system [40] and will not be further explained within this work.

Based on that, the observed area $A_{u,v}(L_{u,v})$ per detector element (u, v) can be calculated by the inverse camera model $\{K_{cam}^{-1}, \delta_{dis}^{-1}\}$ and the respective measured distance $L_{u,v}$. In case, one can assume full crossover between transmitter and receiver frustum ($\xi(L_{u,v}) = 1$), the observed area equals the illuminated area in that region and $A_{t,u,v}(L_{u,v}) = A_{u,v}(L_{u,v})$. For the investigated Flash LiDAR system, the measurement distance to full crossover $L_{\xi=1}$ based on given design parameters, was calculated to be less than the minimum detection range of 0.5 m. Therefore, the assumption can be seen as reasonable in this case.

The peak power portion $P_{0,u,v}$ transmitted to the observed area $A_{u,v}(L_{u,v})$ can be calculated by the radiant intensity profile of the transmitter. In case, the beam profile is modeled ideal, i.e., the transmitted peak power is uniformly distributed, and the illuminated frustum covers exactly the observed frustum, the peak power can be divided equally on the areas $A_{u,v}(L_{u,v})$ as implemented by Sun et al. [37]. Therefore, the respective peak power can be calculated by $P_{0,u,v} = \frac{P_0}{W \cdot H}$ with W and H being the horizontal and vertical number of photosensitive elements, respectively.

Assuming homogeneous precipitation characteristic over the sensor's field of view, the received power of a single photosensitive element, can finally be expressed by:

$$P_{r,u,v} = \underbrace{C_A P_{0,u,v} \tau_h}_{system} \underbrace{\frac{1}{L_{u,v}^2}}_{geometric} \underbrace{H_{T,u,v}(L_{u,v}) T^2(L_{u,v})}_{attenuation} \quad (8)$$

with $T(L_{u,v})$ depending on α integrated over target distance and $H_{T,u,v}(L_{u,v})$ depending on the target nature.

F. Discussion

One can clearly see, that under the given assumption of a Dirac-shaped transmit pulse (see (2)), the equation offers a closed-form solution. Furthermore, the geometric and system part of (8) can be calculated decoupled from the attenuation part and therefore, an ideal return signal with $\alpha = 0$ and $\beta = \beta_{0,u,v}$ from measurement or simulation can simply be postprocessed by multiplication with the respective transmission loss $T^2(L_{u,v}, \alpha \neq 0)$. However, this does not hold for a raytracing simulation considering multiple hits, i.e., indirect reflections, since the transmission loss between two consecutive hit points must be taken into account when solving the recursive raytracing equation [25]. In this case, transmission loss has to be directly considered within the raytracing simulation.

As mentioned before, the target response on the other hand can, as superposition of the hard and soft target response, describe the power fraction which is backscattered from the target and the volumetric particle distribution, respectively. By this though, the equation does not include the direct reflection from large particles which are close to the sensor and cover the aperture of one or several photosensitive elements. This effect is especially severe if the transmitter aperture as well as the distance between transmitter and receiver axis are small, which is in fact common for automotive sensors and was broadly demonstrated for scanning LiDARs within previous works, presented in Section II. As a contribution, this effect is additionally demonstrated for a Flash LiDAR system by exemplary measurement results, discussed in Section V. Therefore, a probabilistic modeling approach as suggested by Kilic et al. [19] is required, which can be added as probabilistic term

$$H_{T,u,v}^X(L^X) = \beta_{u,v}^X(L^X) = f(Q_b(D^X), D^X, L^X) \quad (9)$$

describing the stochastic appearance of particles in a distance L^X with respective backscattering efficiency $Q_b(D^X)$ and diameter D^X sampled from the measured size distribution $N(D)$.

IV. MEASUREMENT SETUP

Within this section, the outdoor measurement setup as well as the sensor under test (SUT) are described, e.g., in this paper a Continental Flash LiDAR sensor. The general setup consists of two independent units – a perception sensor unit (PSU) with a reference RGB camera as well as the SUTs and a weather sensor unit (WSU) which acquires data once every 60 s (see Fig. 3). Both units are remotely connected over a cloud-computing platform in order to mount and operate them independently from each other while being able to store and visualize the data online.

A. WSU

The WSU mainly includes measurement instruments from the manufacturer *Thies Clima* to characterize wind, temperature, air humidity, as well as sun irradiance and precipitation conditions. The latter, which is in the focus of this work, is measured by a laser disdrometer [41], capable of identifying

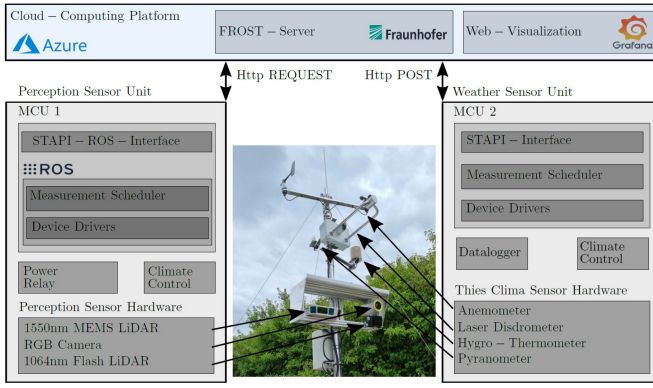


Fig. 3. Outdoor infrastructure setup consisting of a perception sensor unit with the devices under test and a weather sensor unit for continuous acquisition of precise weather data. Both systems are connected to a cloud-computing platform in order to exchange, store and visualize the respective data online.

and counting the occurring particle types (snow, rain and hail) as well as their size and velocity over an integration time t_{int} .

Based on the raw disdrometer data, one can estimate α and β by discrete integration over the captured particle characteristics. Generally, the disdrometer counts particles with a specific velocity v and diameter D and saves it into a discrete 2D histogram $n(I \times J)$ with velocity bins j and diameter bins i , each with a width Δv_j , ΔD_i and a nominal value v_j , D_i . An exemplary particle spectrum for a precipitation rate of $R = 21 \frac{\text{mm}}{\text{h}}$ is shown in Fig. 4. These distributions can strongly vary with the location and corresponding type of precipitation [42], [43].

The particles are counted over an integration time t_{int} (typically 60 s, as in our case) in a detector cross section A_{det} (in our case 0.00456 m^2). Now, in order to normalize n to the average number of particles per unit volume $N(D_i)$, the following transformation can be conducted [41], [44]:

$$N(D_i) = \frac{n_i^{\sum j}}{\bar{v}_i \cdot t_{int} \cdot A_{det} \cdot \Delta D_i} \quad (10)$$

with $n_i^{\sum j}$ being the sum of all particles in diameter bin i and \bar{v}_i being the average particle velocity in diameter bin i . By that, (6) can be calculated discretely by the wavelength and particle diameter dependent $Q_{ext}(D)$:

$$\alpha \approx \hat{\alpha} = \frac{\pi}{4 \cdot t_{int} \cdot A_{det}} \sum_{i=1}^I D_i^2 Q_{ext}(D_i) \frac{n_i^{\sum j}}{\bar{v}_i} \quad (11)$$

and (7) accordingly by replacing $Q_{ext}(D_i)$ with $Q_b(D_i)$.

Opposed to the wavelength dependent backscattering and extinction coefficient, the disdrometer is able to derive precipitation rate and sum directly with an error of less than 15 % in case of rain. Since, besides precipitation, also sun irradiance, wind, temperature and humidity are recorded, the WSU also allows to focus in future works for example on modeling the measurement interference caused by sun irradiance, as well as temperature induced pixel noise.

The overall WSU result data is generally collected and posted to the cloud service by an additional main computing unit (MCU) using the OGC Sensor Things API (STAPI) [45],

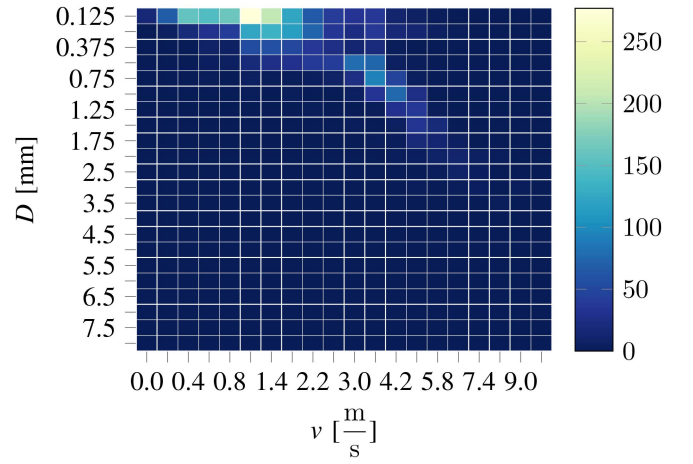


Fig. 4. Number of particles n with a diameter D and a velocity v for a measured precipitation rate of $R = 21 \frac{\text{mm}}{\text{h}}$.

while the live Web visualization is realised by Grafana dashboards.

B. PSU

The PSU on the other hand, frequently polls the current weather state from the server in order to check whether an unobserved adverse weather condition, e.g., in form of a specific precipitation rate, occurs. In this case, the MCU is booting all SUTs to take a datasample of a few seconds, saving it locally and eventually shifting it to the cloud. By that, it is aimed for achieving a balanced dataset while keeping overall data amount manageable. For automation and standardized perception sensor data handling, the MCU including all sensor and device drivers are working on the well-known, open robot operating system (ROS). In this manner, the PSU can be flexibly extended by further SUTs in the form of LiDAR, camera or Radar sensors.

In general, it can also be utilized within smart city applications as static infrastructure installation for traffic monitoring and control. Object information including the trajectories and count of vehicles, pedestrians, cyclists and other vulnerable road users can be accessed by the installed camera and LiDAR sensors and transmitted to the backend cloud platform in an anonymous manner via the STAPI interface. In this manner, it can additionally be used to calibrate microscopic traffic models as well as behavior models of vulnerable road users and drivers.

Coming to the sensor hardware, a *micro-electro-mechanical system* (MEMS) scanning LiDAR from Neuvention, an automotive Flash LiDAR system from Continental and an additional reference RGB camera are currently installed in the PSU (see Fig. 3, left). However, since, this work focuses on Flash LiDAR sensors, the Continental system is investigated as SUT in the following. It is a direct time-of-flight sensor, which provides depth and intensity images, as well as an equivalent point cloud by evaluating the pixel-wise pulse return time and intensity in a resolution of 128×32 pixel with a frame rate of up to 25 Hz. It operates on a wavelength of 1064 nm with a field of view of $120^\circ \times 27.5^\circ$, covering a measurement range from

0.5 m to 25 m. It is worth mentioning that, within this work, only the first LiDAR return pulse was considered in each pixel. Generally, a large number of today's LiDARs, including the SUT, offer a multi echo capability. By this, a possible reflection from the actual target can be processed in addition to the precipitation or fog induced false positive detection.

V. RESULTS

The datasets from a first measurement period were recorded under observation of a static scene in form of an outdoor measurement area. The goal is to investigate the effects of varying precipitation conditions on the SUT performance and to quantify the resulting degradation effects. Furthermore, the LiDAR's precipitation induced signal attenuation α is calculated based on the WSU results and scattering theory introduced in Section III. The results are compared to earlier research and the respective intensity loss are discussed with respect to the observed signal attenuation of the SUT, as well as to the findings of earlier LiDAR tests under artificial precipitation.

The results presented here were collected over a measurement period of approximately three months with the majority of measurements conducted with a precipitation rate R of less than $25 \frac{\text{mm}}{\text{h}}$. Since, only rain is considered within this work, mixed or solid precipitation events like hail were filtered out during the evaluation.

A. WSU

To parameterize the precipitation induced transmission loss, the extinction coefficient α was calculated by (11), based on the spectrum of the respective precipitation event (see Fig. 4). In Fig. 5 the resulting extinction coefficient is plotted over the respective precipitation rate and fitted with respect to an exponential relationship as recommended by ITU-R [43]:

$$\alpha = a \cdot R^b \quad (12)$$

with a and b being empiric fitting parameters. Moreover, well-known parameterizations, which were found by earlier works of Carbonneau [46], as well as Hiromoto [47] and Akiba et al. [48] were plotted next to it.

As one can see, all functions show deviations, especially for higher precipitation rates. This is due to the reason that the precipitation spectrum and resulting extinction coefficient are highly dependent on the measuring location and its local precipitation characteristics [43]. The empiric functions of the previous works offer a good example, with the underlying data being gathered in Japan and France, respectively.

Another reason for the steeper increase of the fitted function is the fact that the measurement data is not yet as dense under high precipitation rates (see Fig 5, lower chart) and therefore, the function fit is not as trustworthy in this region as for lower precipitation rates.

Looking at the results, one can see that the volumetric signal extinction is remarkable, even in case a low range LiDAR with a measurement range of 25 m is considered. Thus, depending on the specific precipitation characteristics, the signal is attenuated between 0.65 dB and 1.1 dB on a two-way distance of

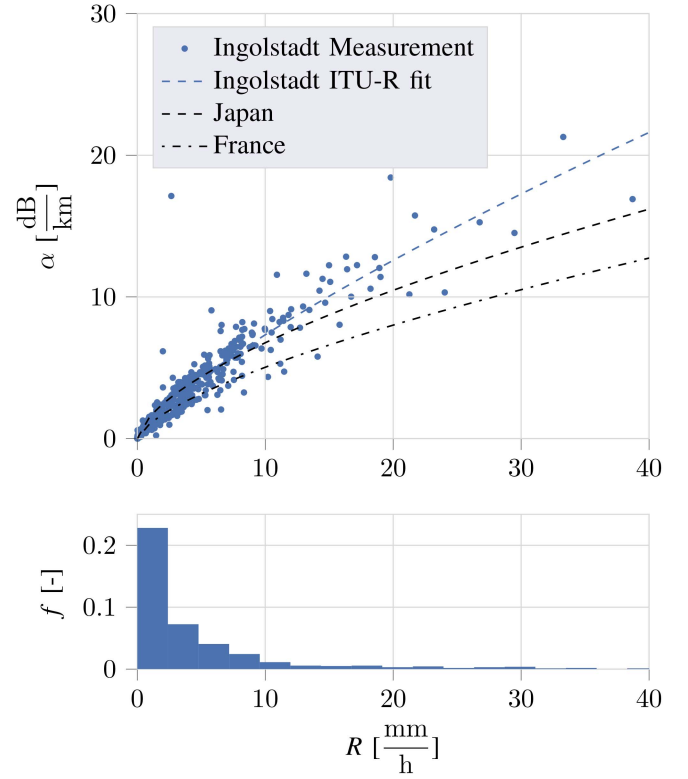


Fig. 5. The upper figure shows the extinction coefficient α for a wavelength $\lambda = 1064 \text{ nm}$ over the respective measured precipitation rate R including an exponential function fit with respect to the ITU-R recommendation [43]. Additionally, corresponding parameterizations for precipitation measurements in France [46] and Japan [47], [48] are illustrated for reference. In the lower image one can see the density histogram of recorded precipitation events with respect to R .

50 m and a strong rain rate of $R = 40 \frac{\text{mm}}{\text{h}}$. This again results in an intensity decrease between 13.6 % and 22 % if converted from specific attenuation in $\frac{\text{dB}}{\text{km}}$ to the path loss in $\frac{1}{m}$ and inserted into (3).

These considerations are underlined by results from Montalban et al. [11]. The authors measured among other things the mean intensity decrease (signal attenuation) and standard deviation under varying artificial rain rates with a static target in 23 m. For a rain rate of $R = 40 \frac{\text{mm}}{\text{h}}$ they even observed an intensity decrease between 25 % to 60 % for different tested sensors. This comparatively strong attenuation could be verified by measurements with the Flash LiDAR sensor (see Section V-B) and may result from the fact that the power loss from volumetric backscattering with respect to (7) is not yet considered.

B. PSU

Representative data samples of the Flash LiDAR in case of dry and rainy weather are shown in Fig. 6, each with a reference RGB image of the static scene (a), as well as the corresponding intensity image (b) and point cloud (c) from the SUT. By qualitative comparison, one can generally identify a loss of detections on the wet street as well as for occurring puddles, since the incident laser beam is reflected in a specular manner with no sufficiently strong signal returning to the

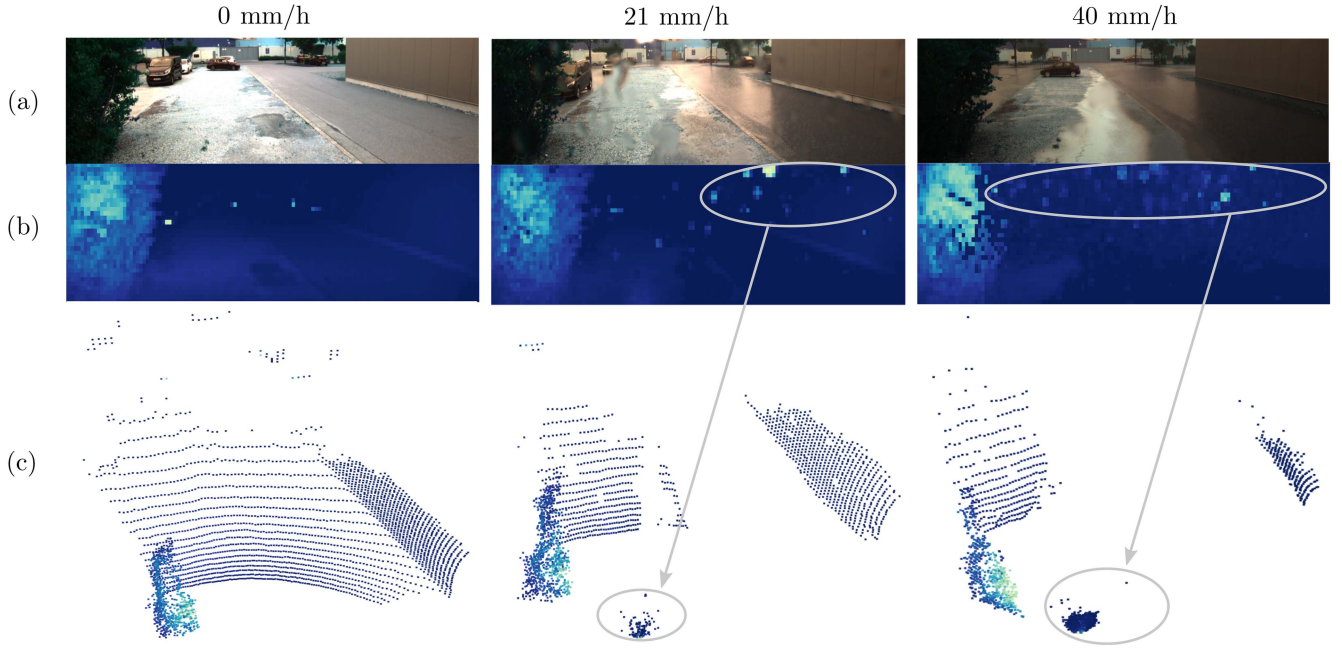


Fig. 6. Data sample of the Flash LiDAR sensor's first return pulse with no precipitation (left) as well as with a precipitation rate of $R = 21 \frac{\text{mm}}{\text{h}}$ (middle) and $R = 40 \frac{\text{mm}}{\text{h}}$ (right). In the upper images (a), the static scene is shown in a reference RGB image, while in the middle and lower image, the respective intensity frames (b) and corresponding point clouds (c) from the SUT are illustrated. The LiDAR data degradation with increasing precipitation is clearly recognizable.

sensor. More importantly, one can detect the two major degradation effects, which were also observed by previous works with focus on scanning LiDARs: First, one can see an overall intensity reduction by rain caused signal attenuation and second, a high number of false positive detections close to the sensor aperture, both leading to a reduction of effective measurement range.

The former can be confirmed by examining the relative signal intensity of every detection in the scene with respect to its distance. In order to reduce measurement noise, a time series of $k = 1 \dots K = 300$ static depth and intensity frames was taken for each recorded precipitation event to calculate the pixel-wise temporal mean of the normalized intensity \bar{I}_{rel} and depth \bar{L} :

$$\bar{I}_{\text{rel}}(u, v) = \frac{1}{K} \sum_{k=1}^K \frac{I(u, v)}{I_{\text{max}}} \quad (13)$$

and

$$\bar{L}(u, v) = \frac{1}{K} \sum_{k=1}^K L(u, v) \quad (14)$$

with (u, v) being the pixel coordinates as described in Section III. The results for selected rain rates are illustrated in Fig. 7. It can be seen, that with increasing precipitation, the backscattered signal intensity is globally decreasing. Furthermore, less points are measured in higher distances.

In order to quantify the intensity decline from dry conditions to a precipitation rate of $R = 40 \frac{\text{mm}}{\text{h}}$, a distance of $L = 5$ m and $L = 10$ m was evaluated, resulting in a mean intensity decrease of 40 % and 60 %, respectively. Thus, the measurement results match with previous results from scanning LiDARs [11].

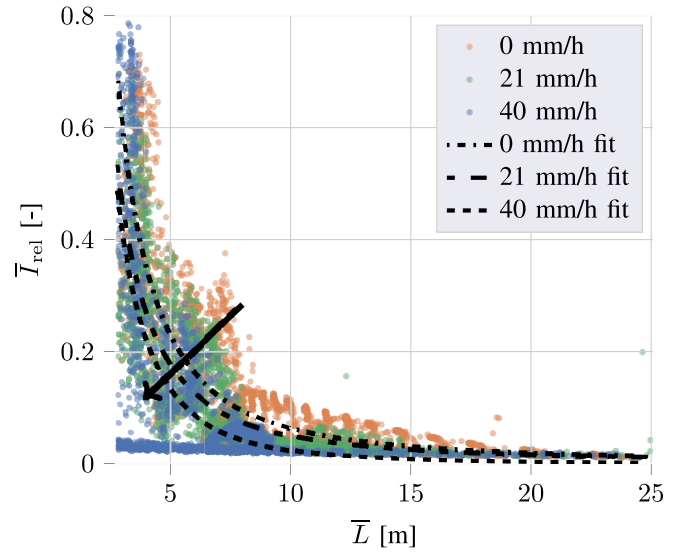


Fig. 7. Relative mean intensity \bar{I}_{rel} and distance \bar{L} of detections in the static scene under varying precipitation rate from $R = 0 \frac{\text{mm}}{\text{h}}$ to $R = 40 \frac{\text{mm}}{\text{h}}$. One can see, that the intensity and measurement range is globally decreasing with increasing precipitation rate.

Besides the overall signal attenuation, one can in particular identify an increasing number of wrong detections caused by direct backscattering from large raindrops. This effect is especially severe in a range of less than 1 m in front of the sensor. In this case, the high irradiance acting onto the raindrops, as well as the small angle between transmitter and receiver, lead to a sufficiently high amount of backscattered power to trigger a faulty detection and in some cases even saturating the respective photosensitive element. In the resulting intensity frames this effect can be observed as stochastically distributed image

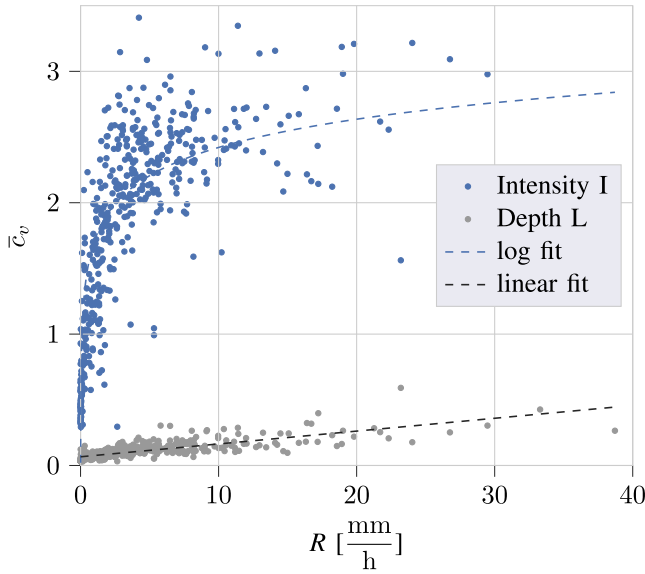


Fig. 8. Spatial mean of temporal coefficient of variation \bar{c}_v for depth and intensity measurements under purely liquid precipitation. Both images show a strong positive trend with increasing precipitation rate R .

artifacts (see Fig. 6 (b)) and as noise in the corresponding point cloud (see Fig. 6 (c)).

To quantify the resulting spatio-temporal noise for varying rain rates, the coefficient of variation c_v [49] is used as a metric. Since, it expresses the standard deviation of a dataset with respect to its corresponding mean, it offers the possibility to compare noise among different sensors with different measurement ranges and quantization. Based on the work of Bijelic et al. [50], also the mean Shannon Entropy of the intensity and depth frames is evaluated, but turned out to be a less strong feature to describe data degradation by rain, than by fog.

In order to calculate c_v , again, a time series of $K = 300$ static depth and intensity frames was extracted for each recorded precipitation rate to calculate $\bar{I}_{\text{rel}}(u, v)$ and $\bar{L}(u, v)$, as well as the corresponding standard deviations $\sigma_{I,\text{rel}}(u, v)$ and $\sigma_L(u, v)$. To finally collapse the resulting pixel-wise temporal coefficient of variation to one numeric value per precipitation rate, the spatial mean over all pixels was calculated:

$$\bar{c}_{v,I} = \frac{1}{W \cdot H} \sum_v \sum_u \frac{\sigma_{I,\text{rel}}(u, v)}{\bar{I}_{\text{rel}}(u, v)} \quad (15)$$

and

$$\bar{c}_{v,L} = \frac{1}{W \cdot H} \sum_v \sum_u \frac{\sigma_L(u, v)}{\bar{L}(u, v)} \quad (16)$$

The results of the first measurement period are illustrated in Fig. 8. One can clearly see, that with rising rain rate, the noise in measured intensity and depth due to false detections is strongly increasing – In case of the intensity up to approximately 350 %.

Based on the previously mentioned measurement results of Montalban et al. [11], one can calculate a respective intensity

variation between 40 % and 75 %, depending on the sensor. The comparatively strong difference results mainly from the fact that the authors measure the variation in intensity only based on points which are covering a static Lambertian target with 80 % reflectivity in a fixed target distance, while in this work, the sensor's whole field of view including different target distances and materials with different, rather low reflectivities are considered (see Fig. 6). Since, the difference between the high intensity which is reflected by rain drops and the low intensity which is reflected by low-reflective materials, is much larger than the difference between the intensity from the high-reflective target and the reflected intensity from the rain drops, also the coefficient of variation is much larger and cannot be compared directly. This emphasises the need for standardized reflection targets for further testing and model calibration.

Nevertheless, both results show that the effect of false positive detections can be considered as a significant source of precipitation induced data degradation in LiDAR systems and cannot be neglected within weather model development. Solely considering the volumetric signal attenuation is not sufficient to accurately model precipitation effects and a probabilistic model extension as discussed in Section III-F has to be utilized.

VI. CONCLUSION

In this work, a mathematical modeling approach for a Flash LiDAR sensor considering adverse weather effects is introduced. Additionally, an in-field test setup for automated recording of time-correlated weather and LiDAR data including results of a first measurement period are presented. By that, precipitation-induced data degradation of the tested Flash LiDAR sensor is evaluated in a quantitative manner and compared to previous works by measuring the volumetric signal attenuation and calculating the pixel-wise temporal coefficient of variation in depth and intensity for varying rain rates between 0 and 40 $\frac{\text{mm}}{\text{h}}$. The results show that next to the precipitation induced signal attenuation, especially the false positive detections due to large, sensor close particles lead to severe degradation which has to be considered within model development.

In subsequent works, the proposed stochastic model for the occurrence of large, sensor close particles will be developed based on the measured precipitation characteristics and LiDAR data. Finally, the model will be embedded in a real time capable raytracing simulation and validated under varying precipitation conditions by reference measurements of standardized Lambertian targets with defined differential reflectivity. Furthermore, the model will be gradually extended by other environmental effects like sun irradiance, snow and fog.

REFERENCES

- [1] M. C. Galassi and A. Lagrange, *New Approaches for Automated Vehicles Certification Part I, Current and Upcoming Methods for Safety Assessment*. Luxembourg City, Luxembourg: Publ. Office Eur. Union, 2020.
- [2] R. Donà and B. Ciuffo, "Virtual testing of automated driving systems. A survey on validation methods," *IEEE Access*, vol. 10, pp. 24349–24367, 2022.

- [3] S. Hafner, "Physical modeling of environment detection sensors, based on GPU-supported shader technology," in *Proc. 15th Internationales Stuttgarter Symp.*, 2015, pp. 769–788.
- [4] N. Hempe, *Bridging the Gap Between Rendering and Simulation Frameworks: Concepts, Approaches and Applications for Modern Multi-Domain VR Simulation Systems*. Wiesbaden, Germany: Springer Fachmedien Wiesbaden, 2016.
- [5] F. Rosique, P. J. Navarro, C. Fernández, and A. Padilla, "A systematic review of perception system and simulators for autonomous vehicles research," *Sensors*, vol. 19, no. 3, p. 648, 2019.
- [6] M. Bijelic, T. Gruber, and W. Ritter, "A benchmark for Lidar sensors in fog: Is detection breaking down?" in *Proc. IEEE Intell. Veh. Symp. (IV)*, 2018, pp. 760–767.
- [7] S. Hasirlioglu, I. Doric, A. Kamann, and A. Riener, "Reproducible fog simulation for testing automotive surround sensors," in *Proc. IEEE 85th Veh. Technol. Conf. (VTC Spring)*, Jun. 2017, pp. 1–7.
- [8] R. Heinzler, P. Schindler, J. Seekircher, W. Ritter, and W. Stork, "Weather influence and classification with automotive Lidar sensors," in *Proc. IEEE Intell. Veh. Symp. (IV)*, 2019, pp. 1527–1534.
- [9] M. Jokela, M. Kutila, and P. Pykönen, "Testing and validation of automotive point-cloud sensors in adverse weather conditions," *Appl. Sci.*, vol. 9, no. 11, p. 2341, 2019.
- [10] M. Kutila, P. Pykönen, H. Holzhuter, M. Colomb, and P. Duthon, "Automotive Lidar performance verification in fog and rain," in *Proc. 21st Int. Conf. Intell. Transp. Syst. (ITSC)*, Nov. 2018, pp. 1695–1701.
- [11] K. Montalbano, C. Reymann, D. Atchuthan, P.-E. Dupouy, N. Riviere, and S. Lacroix, "A quantitative analysis of point clouds from automotive Lidars exposed to artificial rain and fog," *Atmosphere*, vol. 12, no. 6, p. 738, 2021.
- [12] A. Mayra, E. Hietala, M. Kutila, and P. Pykönen, "Spectral attenuation in low visibility artificial fog: Experimental study and comparison to literature models," in *Proc. 13th IEEE Int. Conf. Intell. Comput. Commun. Process. (ICCP)*, Sep. 2017, pp. 303–308.
- [13] L. Daniel, D. Phippen, E. Hoare, A. Stove, M. Cherniakov, and M. Gashinova, "Low-THz radar, Lidar and optical imaging through artificially generated fog," in *Proc. Int. Conf. Radar Syst. (Radar)*, 2017, pp. 1–4.
- [14] S. Hasirlioglu, A. Kamann, I. Doric, and T. Brandmeier, "Test methodology for rain influence on automotive surround sensors," in *Proc. IEEE 19th Int. Conf. Intell. Transp. Syst. (ITSC)*, Nov. 2016, pp. 2242–2247.
- [15] I. I. Kim, B. McArthur, and E. J. Korevaar, "Comparison of laser beam propagation at 785 nm and 1550 nm in fog and haze for optical wireless communications," in *Proc. Opt. Wireless Commun. III*, 2001, pp. 26–37.
- [16] R. H. Rasshofer, M. Spies, and H. Spies, "Influences of weather phenomena on automotive laser radar systems," *Adv. Radio Sci.*, vol. 9, pp. 49–60, Jul. 2011.
- [17] C. Goodin, D. Caruth, M. Doude, and C. Hudson, "Predicting the influence of rain on LIDAR in ADAS," *Electronics*, vol. 8, no. 1, p. 89, 2019.
- [18] M. Hahner, C. Sakaridis, D. Dai, and L. van Gool, "Fog simulation on real LiDAR point clouds for 3D object detection in adverse weather," in *Proc. IEEE/CVF Int. Conf. Comput. Vis. (ICCV)*, 2021, pp. 15263–15272.
- [19] V. Kilic, D. Hegde, V. Sindagi, A. B. Cooper, M. A. Foster, and V. M. Patel, "Lidar light scattering augmentation (LISA): Physics-based simulation of adverse weather conditions for 3D object detection," 2021, *arXiv:2107.07004*.
- [20] S. Hasirlioglu and A. Riener, "A model-based approach to simulate rain effects on automotive surround sensor data," in *Proc. 21st Int. Conf. Intell. Transp. Syst. (ITSC)*, Nov. 2018, pp. 2609–2615.
- [21] Y. Zhao, T. K. Lea, and R. M. Schotland, "Correction function for the Lidar equation and some techniques for incoherent CO(2) Lidar data reduction," *Appl. Opt.*, vol. 27, no. 13, pp. 2730–2740, 1988.
- [22] J. Kostamovaara et al., "On laser ranging based on high-speed/energy laser diode pulses and single-photon detection techniques," *IEEE Photon. J.*, vol. 7, no. 2, pp. 1–15, Apr. 2015.
- [23] K. Sassen and G. C. Dodd, "Lidar crossover function and misalignment effects," *Appl. Opt.*, vol. 21, no. 17, pp. 3162–3165, 1982.
- [24] T. Halldórsson and J. Langerholc, "Geometrical form factors for the Lidar function," *Appl. Opt.*, vol. 17, no. 2, pp. 240–244, 1978.
- [25] E. Haines and T. Akenine-Möller, *Ray Tracing Gems: High-Quality and Real-Time Rendering with DXR and Other APIs*. Berkeley, CA, USA: Apress, 2019.
- [26] M. Bass, *Handbook of Optics*, 2nd ed. New York, NY, USA: McGraw-Hill, 2001.
- [27] S. Hasirlioglu and A. Riener, "Introduction to rain and fog attenuation on automotive surround sensors," in *Proc. IEEE 20th Int. Conf. Intell. Transp. Syst. (ITSC)*, Oct. 2017, pp. 1–7.
- [28] R. Roriz, J. Cabral, and T. Gomes, "Automotive LiDAR technology: A survey," *IEEE Trans. Intell. Transp. Syst.*, vol. 23, no. 7, pp. 6282–6297, Jul. 2022.
- [29] H. C. de van Hulst, *Light Scattering by Small Particles* (Dover Books on Physics). New York, NY, USA: Dover Publ. Inc., 2018.
- [30] G. Mie, "Beiträge zur optik trüber medien, speziell kolloidaler metallösungen," *Annalen der Physik*, vol. 330, no. 3, pp. 377–445, 1908.
- [31] D. Deirmendjian, *Light Scattering on Spherical Polydispersions*. New York, NY, USA: Amer. Elsevier, 1969.
- [32] J. S. Marshall and W. M. K. Palmer, "The distribution of raindrops with size," *J. Meteorol.*, vol. 5, no. 4, pp. 165–166, 1948.
- [33] G. Feingold and Z. Levin, "The lognormal fit to raindrop spectra from frontal convective clouds in Israel," *J. Climate Appl. Meteorol.*, vol. 25, no. 10, pp. 1346–1363, 1986.
- [34] R. Nebuloni and C. Capsoni, "Laser attenuation by falling snow," in *Proc. 6th Int. Symp. Commun. Syst. Netw. Digit. Signal Process.*, 2008, pp. 265–269.
- [35] J. A. Smith, E. Hui, M. Steiner, M. L. Baeck, W. F. Krajewski, and A. A. Ntelekos, "Variability of rainfall rate and raindrop size distributions in heavy rain," *Water Resour. Res.*, vol. 45, no. 4, pp. 1–12, 2009.
- [36] F. Gaudfrin, O. Pujol, R. Ceolato, G. Huss, and N. Riviere, *A New Lidar Inversion Method Using a Surface Reference Target. Application to the Backscattering Coefficient and Lidar Ratio Retrievals of a Fog-Oil Plume at Short-Range*, Eur. Geosci. Union, Munich, Germany, 2019.
- [37] J. Sun, J. Liu, and Q. Wang, "A multiple-slit streak tube imaging Lidar and its detection ability analysis by flash Lidar equation," *Optik*, vol. 124, no. 3, pp. 204–208, 2013.
- [38] Q. Wang, J. Wei, J. Sun, and J. Gao, "Non-scanning imaging laser Lidar equation," in *Proc. Int. Conf. Optoelectron. Microelectron. (ICOM)*, 2012, pp. 217–220.
- [39] R. Hartley and A. Zisserman, *Multiple View Geometry in Computer Vision*, 2nd ed. Cambridge, U.K.: Cambridge Univ. Press, 2015.
- [40] M. Kettelgerdes, L. Böhm, and G. Elger, "Correlating intrinsic parameters and sharpness for condition monitoring of automotive imaging sensors," in *Proc. 5th Int. Conf. Syst. Rel. Safety (ICSRS)*, 2021, pp. 298–306.
- [41] (Adolf Thies GmbH & Co. KG, Göttingen, Germany). *Laser Precipitation Monitor 5.4110.xx.x00: Instructions for Use*. (2021).
- [42] J. Ryu, H.-J. Song, B.-J. Sohn, and C. Liu, "Global distribution of three types of drop size distribution representing heavy rainfall from GPM/DPR measurements," *Geophys. Res. Lett.*, vol. 48, no. 3, 2021, Art. no. e2020GL090871.
- [43] L. A. R. da Silva Mello and T. Tjelta, Eds., *Handbook Radiowave Propagation Information for Designing Terrestrial Point-to-Points Links*, 2008th ed. Geneva, Switzerland: ITU, 2009.
- [44] R. Acharya, "Tropospheric impairments: Measurements and mitigation," in *Satellite Signal Propagation, Impairments and Mitigation*. London, U.K.: Elsevier, 2017, pp. 195–245.
- [45] S. Liang, C.-Y. Huang, and T. Khalafbeigi, *OGC Sensorthings API Part 1: Sensing, Version 1.0*, Standard OGC 15-078r6, 2016.
- [46] T. H. Carbonneau, "Opportunities and challenges for optical wireless communication," in *Proc. SPIE Conf. Opt. Wireless Commun.*, 1998, pp. 119–128.
- [47] N. Hiromoto, "Novel detector technologies for infrared communication and sensing," in *Proc. CRC Int. Topic Workshop Space Laser Commun. Current Status Future Perspect.*, 1997, pp. 90–95.
- [48] M. Akiba, K. Wakamori, and S. Ito, "Measurement of optical propagation characteristics for free-space optical communications during rainfall," *IEICE Trans. Commun.*, vol. E87B, no. 7, pp. 2053–2056, 2004.
- [49] B. Everitt, *The Cambridge Dictionary of Statistics*, 1st ed. Cambridge, U.K.: Cambridge Univ. Press, 1998.
- [50] M. Bijelic et al., "Seeing through fog without seeing fog: Deep multimodal sensor fusion in unseen adverse weather," in *Proc. IEEE/CVF Conf. Comput. Vis. Pattern Recognit. (CVPR)*, 2020, pp. 11679–11689.



Marcel Kettelgerdes received the B.Sc. degree in mechanical engineering from the University of Paderborn in 2016, with strong focus on control engineering and dynamic system modeling and the M.Sc. degree in mechatronics and information technology from Technical University Munich in 2019. He is currently pursuing the Ph.D. degree with the University of Applied Sciences Ingolstadt in close cooperation with Continental. His B.Sc. degree thesis was written in cooperation with Dräger, where he developed a novel anesthetic gas measurement

system based on a more economic data fusion of distributed low-cost sensors. He deepened his knowledge in control engineering and complemented his profile in electrical and software engineering with the Technical University Munich. His research interest lies in the calibration and modeling of optical sensors, with special focus on modeling environmental effects on LiDAR sensors.



Gordon Elger received the degree in physics from the Free University of Berlin, Berlin, in 1998. He worked after his Ph.D. degree as a Scientific Coworker with the Fraunhofer Institute for Reliability and Microintegration (Fraunhofer-IZM Berlin) in the field of optoelectronic, high frequency, and sensor packaging. He joined the Hymite GmbH, Berlin, and became the Team Leader of the backend team developing hermetic packaging technologies for optoelectronics and MEMS. In 2005, he joined the Central RD Department, Electrolux, Italy, as

the Manager of the team for heat and mass transfer, applying and developing Computational Fluid Dynamics and Finite Element Simulations. He returned to Germany and worked for Philips in the Automotive Center, Aachen, focusing on LED packaging and thermal analysis of LED modules. Since 2013, he has been a Professor with the University of Applied Sciences in Ingolstadt (THI) for electronic manufacturing technologies. In 2016, he became a Research Professor leading a Research Group within the field of Microelectronic Packaging. Since 2019, he has also been the Head of the Applied Research Center for “Connected Mobility and Infrastructure” of the Fraunhofer Institute for Transportation and Infrastructure Systems (Fraunhofer-IVI). The core area of his research is optoelectronic, power-electronic, and sensor packaging for automotive applications with focus on reliability assessment and functional safety of the electronic components, modules and systems using physical and data driven modeling. Further his research areas are industry 4.0 and application of machine learning in manufacturing of microelectronic systems, in especially advanced driver assistance systems, sensor modeling and sensor data fusion technologies for ADAS sensor systems for environmental perception.